Article | Received 29 July 2025; Revised 17 September 2025; Accepted 20 September 2025; Published 25 September 2025
https://doi.org/10.55092/bm20250013

Nacre-derived biphasic calcium phosphate composite scaffolds with dual osteogenic/angiogenic potential for efficient bone defect repair

Wenli Dong[1,†], Lujing Zhang[1,†], Kaisheng Wang[1], Yu Zhang[1], Yanni Li[1], Yan Yang[1,*] and Chao Zhou[2,*]

[1] College of Marine Life Sciences, Ocean University of China, Qingdao, China
[2] Qilu Hospital of Shandong University (Qingdao), Qingdao, China

† These authors contributed equally to this work.

* Correspondence authors; Emails: yany@ouc.edu.cn (Y.Y.); 2018120308@mail.sdu.edu.cn (C.Z.).

Highlights:

- A nacre-inspired BCP/SA scaffold with adjustable HAP/β-TCP ratios was designed to replicate the natural bone's organic–inorganic architecture.
- The SH5 scaffold exhibited dual osteoinductive and angiogenic activities, enhancing MC3T3-E1 proliferation and differentiation, as well as promoting HUVEC migration and tube formation.
- In vivo, SH5 significantly repaired cranial bone defects and upregulated osteogenesis-related proteins including OCN, OPN and OPG.

Abstract: A composite scaffold integrating biphasic calcium phosphate (BCP) with sodium alginate (SA) was engineered in this study to facilitate the repair of bone defects. Nacre-derived BCP with different ratios of hydroxyapatite (HAP) to β-tricalcium phosphate (β-TCP)—H5 (50:50) and H3 (30:70)—were combined with SA, cross-linked with calcium ions, and freeze-dried to fabricate three types of scaffolds: SN (SA alone), SH3, and SH5. Characterization revealed high crystallinity, porosity (65%–80%), and a pore size of approximately 100 μm. *In vitro*, SH5 scaffolds promoted MC3T3-E1 cell adhesion, proliferation, and differentiation, significantly enhancing osteogenesis-related gene expression (*COL-1, RUNX-2, ALP, OPN*) and alkaline phosphatase activity, while also supporting HUVEC migration and tube formation. *In vivo*, SH5 scaffolds exhibited superior bone regeneration, mineralization, collagen deposition, and integration with host tissue in a rat cranial defect model, accompanied by strong osteocalcin, osteopontin and osteoprotegerin expression. Experimental findings revealed that the SH5 BCP/SA scaffold possesses outstanding osteoinductive and angiogenic properties, thereby reinforcing its potential to be applied as bone defect repair substitutes.

Keywords: bone tissue engineering; biphasic calcium phosphates; sodium alginate; nacre powder

1. Introduction

Current clinical interventions for bone defect management encompass autologous bone grafts, allogeneic transplants, and a variety of biomaterial-based artificial bone substitutes [1]. However, the use of allogeneic bone grafts from bone banks faces significant challenges such as limited supply, immune responses between patients and donor bones, and potential disease transmission [2]. These limitations have driven increasing demand for artificial bone repair materials, which offer more predictable outcomes and fewer complications.

Nacre powder, derived from the innermost layer of mollusk shells [3], is an inorganic-organic composite material that has attracted considerable attention for its exceptional properties. Composed of approximately 95% inorganic calcium carbonate and 5% organic components, nacre features a unique brick-wall microstructure that imparts remarkable toughness and mechanical strength [4–6]. This structure provides high durability and mechanical properties that have made nacre a popular subject in biomimetic research [7]. Moreover, nacre has demonstrated excellent biocompatibility, osteoinductive, and osteoconductive properties, making it an attractive candidate for bone repair applications. Previous research has shown that when nacre powder is mixed with patient blood and injected into bone defect sites, it promotes bone formation while undergoing biodegradation over time [8]. In simulated body fluid (SBF), nacre surfaces also exhibit enhanced hydroxyapatite (HAP) deposition compared to materials like titanium. Nevertheless, it is widely recognized that the organic constituents of nacre are essential for facilitating HAP crystallization, and their absence greatly diminishes its mineralization capacity [9].

To overcome this limitation, nacre powder is often converted to HAP and utilized for bone repair. Nacre can be transformed into calcium orthophosphates, which reconstruct the bone matrix of mammals and stimulate bone regeneration through self-setting mechanisms. The nacre-based calcium orthophosphates composite demonstrated efficient osteogenic activities and improve bone healing in critical bone defect models [10–12]. HAP is well known for its biocompatibility, osteoconductivity, and osteogenic properties [13,14]. HAP could effectively mimic bone structure and facilitate osseous integration [15]. Despite its benefits, HAP exhibits higher crystallinity than natural bone, leading to enhanced chemical stability and slower *in vivo* degradation rates. HAP degrades at a rate inconsistent with the formation of new bone, thereby reducing its potential for bone repair applications [16].

Beta-tricalcium phosphate (β-TCP) has emerged as a promising alternative bone graft material in recent years due to its dense porous structure, which facilitates vascular infiltration and osteoconductivity [17–19]. β-TCP exhibits a faster degradation rate compared to HAP, which can enhance bone formation through osteoclast-mediated resorption [20,21]. While β-TCP is insoluble at physiological pH, its degradation process occurs through osteoclast-mediated resorption [22–24]. Osteoclasts adhere to the β-TCP surface, causing local acidification and leading to β-TCP dissolution [20]. However, β-TCP materials present challenges such as mechanical weakness and unpredictable degradation rates that can hinder bone regeneration. The degradation rate of β-TCP is not fully controllable, which can either slow down or accelerate bone formation depending on the material's resorption [25]. In addition, the mechanical strength of β-TCP is inferior to that of natural bone tissue, limiting its structural effectiveness in load-bearing applications [26].

Biphasic calcium phosphate (BCP), a composite material that combines HAP and β-TCP, offers a solution by balancing the advantages of both materials [27,28]. BCP allows for tunable mechanical

properties and controlled degradation rates through variations in the HAP:β-TCP ratio [29], making it an attractive material for bone repair While HAP provides high strength and biocompatibility, β-TCP offers rapid resorption and encourages faster bone conduction [30]. This synergistic combination makes BCP a versatile material for applications in bone tissue engineering.

Sodium alginate (SA) is a natural polysaccharide and has gained attention as a potential material for bone tissue engineering owing to its advantageous physicochemical and biological characteristics [31,32]. Structurally similar to glycosaminoglycans, SA exhibits hydrophilicity, biocompatibility, and low immunogenicity, and these biological properties make SA ideal for tissue scaffolds [33–35]. SA readily forms gels with divalent cations and has been widely used in cartilage, bone, and skin tissue engineering. However, pure SA materials lack the necessary mechanical strength and cell adhesion properties for effective bone regeneration [36]. Recent studies have shown that combining SA with calcium phosphates, such as HAP and β-TCP, enhances both mechanical properties and cell adhesion, promoting osteoblast proliferation and differentiation [37]. For example, SA composites with HAP significantly promote osteoblast attachment, growth, and *in situ* mineralization. Similarly, when combined with α-TCP, SA has been shown to improve the compressive and tensile strength of bone cement and significantly enhance rat bone marrow stromal cell (rBMSC) adhesion [38].

This study introduces BCP/SA composite scaffolds, designed by combining nacre-derived BCP with sodium alginate, to generate a bone-mimicking material that reflects the natural organic–inorganic architecture of bone tissue. The composite scaffolds, with different HAP:β-TCP ratios (H5: 50% HAP + 50% β-TCP and H3: 30% HAP + 70% β-TCP), are cross-linked using Ca^{2+} and freeze-dried to achieve an ideal scaffold structure. These scaffolds not only provide excellent mechanical strength but also offer controlled degradation, making them suitable for bone repair applications. The scaffolds were characterized in terms of cyto-compatibility, osteogenic activity, and angiogenic potential *in vitro*. The bone defect repair capability of these scaffolds was further assessed using a rat cranial defect model, showcasing their potential for clinical application in bone tissue engineering (Figure 1).

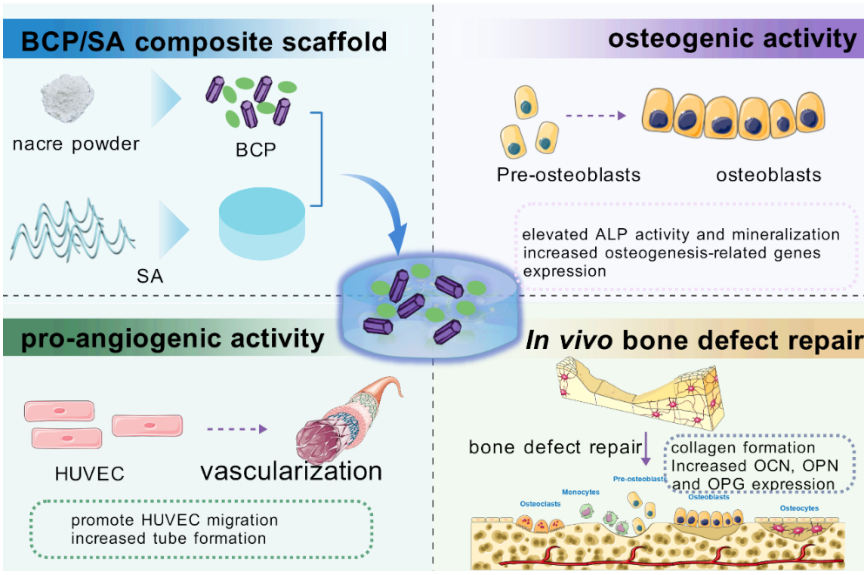

Figure 1. Schematic diagram of the preparation of BCP/SA composite scaffolds and with dual osteogenic/angiogenic potential for efficient bone defect repair.

2. Methods

2.1. Reagents

Nacre powder was obtained from Jisskang. Calcium pyrophosphate was purchased from Aladdin. Triton X-100 was purchased from Sinopharm Chemical Reagent Co., Ltd. Trypsin and DMEM low-glucose medium were purchased from Biological Industries. Bovine serum albumin, BCA protein assay kit, and Masson's trichrome stain were purchased from Solarbio. Fetal bovine serum was purchased from VivaCell. Alkaline phosphatase staining kit, Alizarin Red S staining kit, alkaline phosphatase assay kit, Actin-Tracker Green-488, and Matrix-Gel™ were purchased from Beyotime. β-glycerophosphate sodium and ascorbic acid dexamethasone were purchased from Sigma. DAPI was purchased from Biosharp. TRIzol was purchased from Invitrogen. TB Green® Premix and Ex Taq™ were purchased from TaKaRa. Fastking cDNA Synthesis Kit was purchased from Tiangen.

MC3T3-E1 and Human Umbilical Vein Endothelial Cells (HUVEC) were purchased from the Kunming Cell Bank, Chinese Academy of Sciences (China).

2.2. Preparation of biphasic calcium phosphate (BCP) and characterization

The solid-state reaction conditions between nacre powder and calcium pyrophosphate were improved based on previous literature reports [39]. Nacre powder and calcium pyrophosphate were mixed at a molar ratio of 4:3, and a certain amount of H_2O was added in a ball mill, followed by wet grinding at 25 rps for 1 h. Subsequently, the ground mixture was dried in a vacuum oven at 100 ℃ for 24 h, then calcined at 1000 ℃ for 1 h. By adjusting the amount of H_2O during the wet grinding process, BCP containing different ratios of HAP and β-TCP was prepared and named H3 and H5, respectively. XRD, infrared spectroscopy, and particle size distribution measurements were performed.

2.3. Preparation of BCP/SA composite scaffolds and its characterization

2.3.1. Preparation of BCP/SA composite scaffolds

Different masses of H3, H5, and Nacre were uniformly dispersed in water and ultrasonically dispersed for 10 min. SA was weighed and added to the prepared suspension, then magnetically stirred to get a uniform suspension solution. The suspension was poured into a mold and pre-cooled at −20 °C. The scaffold, after freeze-drying in a freeze dryer (Cryo Mill, Restech), was placed in 10% $CaCl_2$ aqueous solution for crosslinking for 1 h. The excess Ca^{2+} was washed with deionized water, followed by freeze-drying again to obtain the BCP/SA composite scaffolds, which were named SN (1.5% SA + 2.7% Nacre), SH3 (1.5% SA + 2.7% H3), and SH5 (1.5% SA + 2.7% H5).

2.3.2. Swelling ratio measurement of BCP/sodium alginate (BCP/SA) composite scaffolds

The initial dry weight of the BCP/SA scaffolds was recorded as Wi. Subsequently, the samples were immersed in simulated body fluid (SBF) and incubated at 37 °C. At predetermined time intervals (1 min, 3 min, 10 min, 30 min, 12 h, and 24 h), the scaffolds were retrieved, and residual surface fluid was gently removed using absorbent paper. The hydrated weight was then measured and denoted as Ws. The

swelling ratio was determined according to the formula: (Ws − Wi) / Wi × 100%. Each experimental group included a minimum of six replicates, and the data were presented as mean ± standard deviation.

2.3.3. Scaffold porosity determination

The radius and height of the BCP/SA scaffolds were first measured to calculate their volume (V). The initial dry weight of each scaffold was recorded as W1. The samples were then immersed in anhydrous ethanol for 15 min to allow complete penetration, after which they were reweighed (W2). Scaffold porosity (%) was determined using the equation: [(W2 − W1) / (ρV)] × 100%, where W1 denotes the initial weight, W2 the weight after ethanol immersion, ρ the density of anhydrous ethanol, and V the scaffold volume. Each measurement was performed in triplicate, and results were expressed as mean ± standard deviation.

2.3.4. SEM analysis of internal morphology

Freeze-dried scaffolds were longitudinally sectioned at the center using a sterile scalpel. To enhance surface conductivity, the samples were coated with a thin layer of gold. The prepared specimens were mounted on stubs and examined under a scanning electron microscope (SEM, QUANTA 250, FEI, USA) to characterize their internal microstructural features.

2.3.5. Determination of mechanical properties of BCP/SA composite scaffolds

The compressive strength and elastic modulus of the BCP/SA composite scaffolds were evaluated using a universal testing machine (Zwick Z005, Germany). A 10 N compression sensor was employed. Each scaffold was positioned at the center of the testing platform, and the sensor was gradually lowered until it made contact with the specimen. Compression was applied at a constant crosshead speed of 1 mm/min, and the loading was continued until 50% of the original scaffold height was reached. Based on the obtained stress–strain curves, the compressive strength and elastic modulus were calculated.

2.3.6. Cytocompatibility assay of BCP/SA composite scaffolds

The leachate of the BCP/SA composite scaffolds was prepared by immersing the scaffolds in α-MEM medium at a surface area-to-medium volume ratio of 2.2 cm^2/mL, followed by incubation for 72 h. The collected medium was filtered through a 0.22 μm membrane to remove impurities. To obtain the complete leachate medium, fetal bovine serum (FBS, 15%), penicillin–streptomycin solution (1%), ascorbic acid (50 μg/mL), dexamethasone (10 μM), and β-glycerophosphate (10 mM) were added. Control osteogenic induction medium was prepared in parallel without scaffold leachate.

MC3T3-E1 preosteoblasts were obtained from the National Collection of Authenticated Cell Cultures. Cells were maintained in α-MEM medium supplemented with 15% FBS and 1% penicillin–streptomycin, under standard culture conditions (37 °C, 5% CO_2). Passages 3–7 were used for all experiments.

For proliferation analysis, MC3T3-E1 cells were seeded in 96-well plates at a density of 4,000 cells per well. After cell adhesion, the culture medium was replaced with scaffold leachates corresponding to different BCP/SA groups. The control group was cultured in osteogenic induction medium without scaffold leachate, while the blank group contained only α-MEM medium without cells. Each

condition was tested in six replicates. At 24, 48, and 72 h of co-culture, cell proliferation was quantified using the MTT assay. Absorbance was measured at 490 nm using a microplate reader (Multiskan GO 1510, Thermo Fisher Scientific, USA). The relative growth rate (RGR) was calculated as follows: RGR (%) = (OD_{490} experimental group − OD_{490} blank group) / (OD_{490} control group − OD_{490} blank group) × 100%.

2.3.7. Cell viability on BCP/SA composite scaffolds

Scaffolds (10 ×1 mm) were soaked in a cell culture medium for 12 h for re-hydration before cell seeding. MC3T3-E1 cells were seeded onto the BCP/SA scaffold and cultured for 3 and 5 days. The medium was discarded and the cells were washed twice with PBS. Cells were then stained according to the instructions of Calcein/ PI Cell Viability/Cytotoxicity Assay Kit (Beyotime, C2015S). After staining for 1 h, the cells were observed with fluorescence microscope (ECLIPSE Ts2, Nikon).

2.3.8. Cell adhesion on BCP/SA composite scaffolds

MC3T3-E1 cell suspensions were seeded onto each scaffold at a density of 5×10^4 cells per sample. Following 4 h and 24 h of incubation, scaffolds were rinsed with PBS and fixed in 4% paraformaldehyde (Bioshap) for 20 min at room temperature. Samples were subsequently washed twice with distilled water (5 min each). Cell membranes were permeabilized with 0.1% Triton X-100 in PBS for 5 min, followed by blocking with 1% bovine serum albumin (BSA, Solarbio) for 30 min. For cytoskeletal visualization, cells on the scaffolds were stained with Actin-Tracker Green (diluted 1:40–1:200) for 30 min and counterstained with DAPI for 10 min. After two additional PBS washes, the stained cells were imaged using confocal laser scanning microscopy (CLSM, DIC N2, Nikon) with excitation wavelengths set at 488 nm and 633 nm.

2.4. Study on the osteo-inductive activity of composite scaffolds on MC3T3-E1 cells

2.4.1. Effects of composite scaffolds on alkaline phosphatase (ALP) activity in MC3T3-E1 cells

MC3T3-E1 cells were cultured either in control medium or in scaffold leachates to induce osteogenic differentiation. After 7 and 14 days of co-culture, cells were rinsed and fixed in 4% paraformaldehyde. Subsequently, the cells were washed twice with sterile distilled water. ALP activity was visualized using the BCIP/NBT Alkaline Phosphatase Color Development Kit (Beyotime), following the manufacturer's instructions. For quantitative analysis, cells were lysed after washing twice with PBS, and ALP activities were assayed with the Alkaline Phosphatase Assay Kit (Beyotime) according to the protocol indicated by the manufacturer. Total cellular protein was simultaneously quantified using the Nano-300 (Allsheng).

2.4.2. Effects of composite scaffolds on the biomineralization activity of MC3T3-E1 cells

Prior to cell seeding, 12-well culture plates were coated with 0.1% gelatin solution and incubated for 30 min. The gelatin was subsequently removed, and MC3T3-E1 cells were seeded at a density of 4×10^4 cells per well. After 24 h of attachment, the medium was replaced with scaffold leachate in the experimental group or control medium in the control group. Cells were cultured for 14 and 21 days to evaluate biomineralization. At the indicated time points, cells were rinsed three times with PBS and fixed in 4% paraformaldehyde for 20 min at room temperature, followed by two washes with sterile distilled water.

Calcium deposition and extracellular matrix (ECM) mineralization were examined with the Alizarin Red S Staining Kit (Beyotime). For quantitative analysis, 500 μL of 10% cetylpyridinium chloride was added to each well and incubated at 37 °C for 1 h to dissolve calcified nodules. Subsequently, 200 μL of the supernatant from each well was transferred to a 96-well plate, and absorbance was measured at 562 nm using a microplate reader (MULTISKAN GO 1510, Thermo Fisher Scientific, USA).

2.4.3. Effects of composite scaffolds on the osteo-inductive related gene expression of MC3T3-E1 cells

Cells were seeded into 6-well plates and co-cultured with scaffold leachates for the experimental group and control medium for the control group for 14 and 21 days. RNA was extracted using the Trizol method and used for reverse transcription and cDNA amplification on a Mastercycler Nexus X2 (Eppendorf). The primer sequences for GAPDH, RUNX2, OPN, COL1, and ALP genes are listed in Table 1.

MC3T3-E1 cells were seeded into 12-well plates at a density of 1×10^5 cells per well. After 24 h of adhesion, the culture medium was replaced with scaffold leachate in the experimental group and control medium in the control group. Cells were maintained for 14 and 21 days, after which total RNA was extracted using the Trizol reagent (Invitrogen, USA) according to the manufacturer's instructions. RNA concentration and purity were assessed using a NanoDrop spectrophotometer (Thermo Fisher Scientific, USA). Reverse transcription and cDNA synthesis were performed on a Mastercycler Nexus X2 thermal cycler (Eppendorf, Germany). Specific primer sequences targeting GAPDH, RUNX2, OPN, COL1, and ALP are provided in Table 1.

Table 1. Specific primer sequences of genes.

Gene	Forward prime sequence	Reverse prime sequence
GAPDH	TGAACTAACACAGAGGAGGATCAG	GCTTAGGGCATGAGCTTGAC
RUNX 2	ATCCAGCCACCTTCACTTACACC	GGGACCATTGGGAACTGATAGG
OPN	CCAAGCGTGGAAACACACAGCC	GGCTTTGGAACTCGCCTGACTG
COL1	CTGCCCAGAAGAATATGTATCACC	GAAGCAAAGTTTCCTCCAAGACC
ALP	TTTGCTACCTGCCTCACTTCCG	GGCTGTGACTATGGGACCCAG

2.5. Study on the activity of composite scaffolds on HUVEC cells

2.5.1. Effects of composite scaffolds on HUVEC cell 2D migration

HUVEC cells were seeded into 24-well plates at a density of 1×10^5 cells/well. Once the cells adhered and reached 90% confluence, scratch wounds were created in each well. After washing with PBS, the experimental group was treated with the leaching solution of the BCP/SA scaffold (containing 0.2% fetal bovine serum), while the blank group was treated with DMEM medium (also containing 0.2% fetal bovine serum). Cell migration was observed and photographed under an inverted microscope at 0, 12, and 24 h.

2.5.2. Effects of composite scaffolds on HUVEC cell 3D migration

Human umbilical vein endothelial cells (HUVECs) at 70%–80% confluence were serum-starved in medium containing 0.2% fetal bovine serum for 12 h, followed by digestion and centrifugation. Cells were

seeded into the upper chamber of a Transwell insert at a density of 1×10^5 cells per well. The lower chamber was filled with 600 μL of scaffold leachate (experimental group) or DMEM medium (control group). After 12 h of incubation at 37 °C, the medium was discarded, and cells were washed with PBS. Chambers were fixed in methanol for 15 min, rinsed with PBS, air-dried, and stained with 0.1% crystal violet for 20 min. Migrated cells were visualized and imaged under an inverted microscope. For quantitative analysis, the bound dye was eluted with 33% acetic acid, and absorbance was measured at 580 nm.

2.5.3. Effects of composite scaffolds on HUVEC cell angiogenic activity

Following 12 h of serum starvation in medium containing 0.2% fetal bovine serum, HUVECs were seeded into Matrigel-coated 96-well plates at a density of 3×10^4 cells per well. After 4 h of incubation, capillary-like tube formation was observed and imaged using an inverted microscope. Quantitative evaluation of angiogenic activity, including tube length, number of nodes, number of intersections, and number of meshes, was performed using ImageJ software on four randomly selected microscopic fields.

2.6. In vivo bone defect repair functions of composite scaffolds

Specific pathogen-free (SPF) male Sprague–Dawley (SD) rats (200 ± 10 g) were obtained from Ji'nan Pengyue Laboratory Animal Breeding Co., Ltd. (license no. SCXK 2022 0006). Animals were acclimated for one week prior to surgery under standard housing conditions. All experimental protocols were approved by the Animal Ethics Committee of Ocean University of China and conducted in accordance with institutional guidelines. A total of 60 rats were randomized into four groups (n = 15 each) using a blinded allocation method: control, SN, SH3, and SH5. Briefly, four color-coded beads (white = control, yellow = SN, blue = SH3, green = SH5) were placed into an opaque bag, and each rat was randomly assigned by blind drawing.

Rats were anesthetized via intraperitoneal injection of Zoletil (5 mg/kg) and xylazine (15 mg/kg). After shaving and disinfection, animals were fixed in a sterile operating field. A 5-mm circular calvarial defect was created in the parietal bone using a trephine drill. The designated scaffold (according to group allocation) was implanted into the defect site, while the control group received no implant. The bilateral subcutaneous fascia was repositioned and sutured to secure the implant, followed by layered closure of the subcutaneous and skin tissues.

At 1, 2, and 3 months postoperatively, calvarial specimens were harvested and fixed in 4% paraformaldehyde for 24 h. Samples were decalcified in 10% neutral EDTA for approximately one month, dehydrated through graded ethanol (50%–100%), and embedded in paraffin. Longitudinal sections (5 μm) were prepared for histological analysis. Hematoxylin and eosin (H&E) staining was performed to assess general morphology, while collagen deposition was examined using a Modified Masson's Trichrome Staining Kit (Solarbio). Images were acquired with a Nikon Y-TV55 microscope equipped with a Nikon camera (Nikon, Japan). For immunofluorescence analysis, sections were incubated with primary antibodies against OCN, OPN, and OPG (Affinity Biosciences, rabbit, 1:300), followed by goat secondary antibodies (1:500).

At 3 months, bone regeneration was further assessed by micro-computed tomography (Micro-CT, Quantum GX, PerkinElmer). Scanning parameters were set at 100 kV, 120 mA, and 18.2 s scan time.

Reconstructed three-dimensional images were analyzed to quantify bone volume fraction (BV/TV), bone mineral density (BMD), and trabecular pattern factor (Tb.pf).

2.7. Statistical analysis

All data were processed and analyzed using Origin software. Results are presented as mean ± standard deviation (SD). Statistical differences were evaluated using one-way analysis of variance (ANOVA). A p-value < 0.05 was considered statistically significant, $p < 0.01$ as highly significant, and $p < 0.001$ as extremely significant. In all figures, statistical significance is denoted by *, **, and ***, corresponding to $p < 0.05$, $p < 0.01$, and $p < 0.001$, respectively.

3. Results

3.1. BCP characterization results

The characterization results for H3 and H5 were shown in Figure 2. Figure 2A presented the XRD patterns of H3 and H5 compared to standard HAP and β-TCP. Analysis of the XRD patterns using High Score Plus software revealed that H3 consisted of 30% HAP and 70% β-TCP, while H5 comprised 50% HAP and 50% β-TCP. The comparison with standard patterns of HAP (ICDD NO. 09-0432) and β-TCP (ICDD NO. 09-0169) showed that both H3 and H5 samples were free from impurities such as CaO and $CaCO_3$ and exhibited high crystallinity.

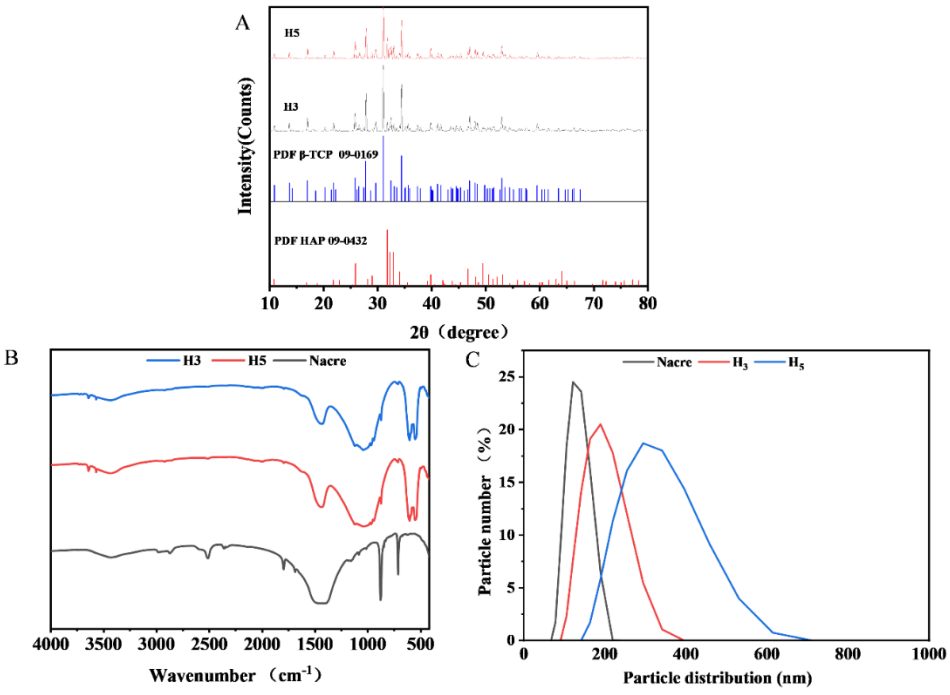

Figure 2. Characterization of BCP. **A.** X-ray diffraction (XRD) patterns of H3 and H5 compared with standard HAP and β-TCP patterns. Analysis confirmed that H3 consists of 30% HAP and 70% β-TCP, while H5 comprises 50% HAP and 50% β-TCP, with both showing high crystallinity. **B.** FTIR spectra of H3, H5, and Nacre, showing characteristic absorption peaks of HAP and β-TCP at 562 cm^{-1}, 610 cm^{-1}, and 1050 cm^{-1}, as well as the CO_3^{2-} peak at 1475 cm^{-1}. **C.** Particle size distribution of BCP scaffolds showing the average particle size range for H3 and H5 samples.

Figure 2B displayed the infrared spectroscopy results for H3, H5, and Nacre. The infrared spectra of H3 and H5 showed characteristic absorption peaks corresponding to HAP and β-TCP. O-P-O bending vibration peaks appeared at 562 cm^{-1} and 610 cm^{-1}, while a prominent P-O stretching vibration peak appeared at 1050 cm^{-1}. The absorption peak at 3437 cm^{-1} was attributed to the -OH bond stretching vibration from residual H_2O. The absorption peak at 1475 cm^{-1} corresponded to the asymmetric stretching vibration of O = C = O, characteristic of CO_3^{2-}.

Figure 2C showed the particle size distribution of Nacre, H3, and H5. The particle size distribution of Nacre displayed a sharp peak, indicating a narrow range of particle sizes, with a large proportion of particles falling within a relatively small size range (around 100 nm). The H3 sample exhibited a broader particle size distribution compared to Nacre, with the peak at a larger particle size (approximately 200 nm) and a wider spread. Similarly, the particle size distribution of H5 was also broader than Nacre's, with the peak appearing at a slightly larger particle size (around 310 nm), indicating that H5 contained a higher proportion of larger particles.

3.2. Characterization results of BCP/SA composite scaffolds

The internal structure and porosity of scaffolds could significantly affect cell adhesion, proliferation, and differentiation on the scaffold surface [40,41]. Scaffolds with appropriate porosity and pore size not only provided support for osteoblasts but also facilitated the transport of nutrients and metabolic waste [42]. Maintaining optimal porosity and pore size could promote the directional differentiation of stem cells into osteoblasts [43]. Figure 3A showed the appearance and scanning electron microscopy (SEM) images of the composite scaffolds. The results demonstrated that all groups exhibited a sponge-like structure, with shapes adaptable to the freeze-drying mold configuration, indicating certain plasticity. The pore size inside the scaffolds was very crucial to affect new bone formation. Pores ranging from several to dozens of micrometers would promote cell adhesion, intracellular signal transduction, cell proliferation, while pores of hundreds of micrometers would facilitate angiogenesis, ECM aggregation, and tissue formation. SEM images revealed that all three composite scaffolds (SN, SH3, and SH5) possessed interconnected porous structures, with internal pore diameters ranging approximately from 90 to 120 μm.

Figure 3B presented the swelling ratio results for the BCP/SA composite scaffolds. All composite scaffolds exhibited rapid water absorption and expansion within 1 min, with swelling ratios increasing quickly, indicating high hydrophilicity and swelling capacity. After 1 min, only the SN group continued to show an increase in the swelling ratio, while the SH3 and SH5 groups reached equilibrium. The porosity measurement results for the composite scaffolds were shown in Figure 3C. The results indicated that SN, SH3, and SH5 all had high porosity, with values of 67%, 78%, and 82%, respectively. The high porosity of these materials suggested large internal specific surface areas and high adsorption capacities, which were beneficial for absorbing tissue exudates from wounds [44]. The compressive stress-strain curve results of the composite scaffolds were shown in Figure 3D. At 80% strain, SH3 and SH5 exhibited compressive stresses of 0.79 MPa and 0.65 MPa, respectively, outperforming SN's 0.3 MPa, with all composite scaffolds meeting the strength requirements for bone tissue engineering.

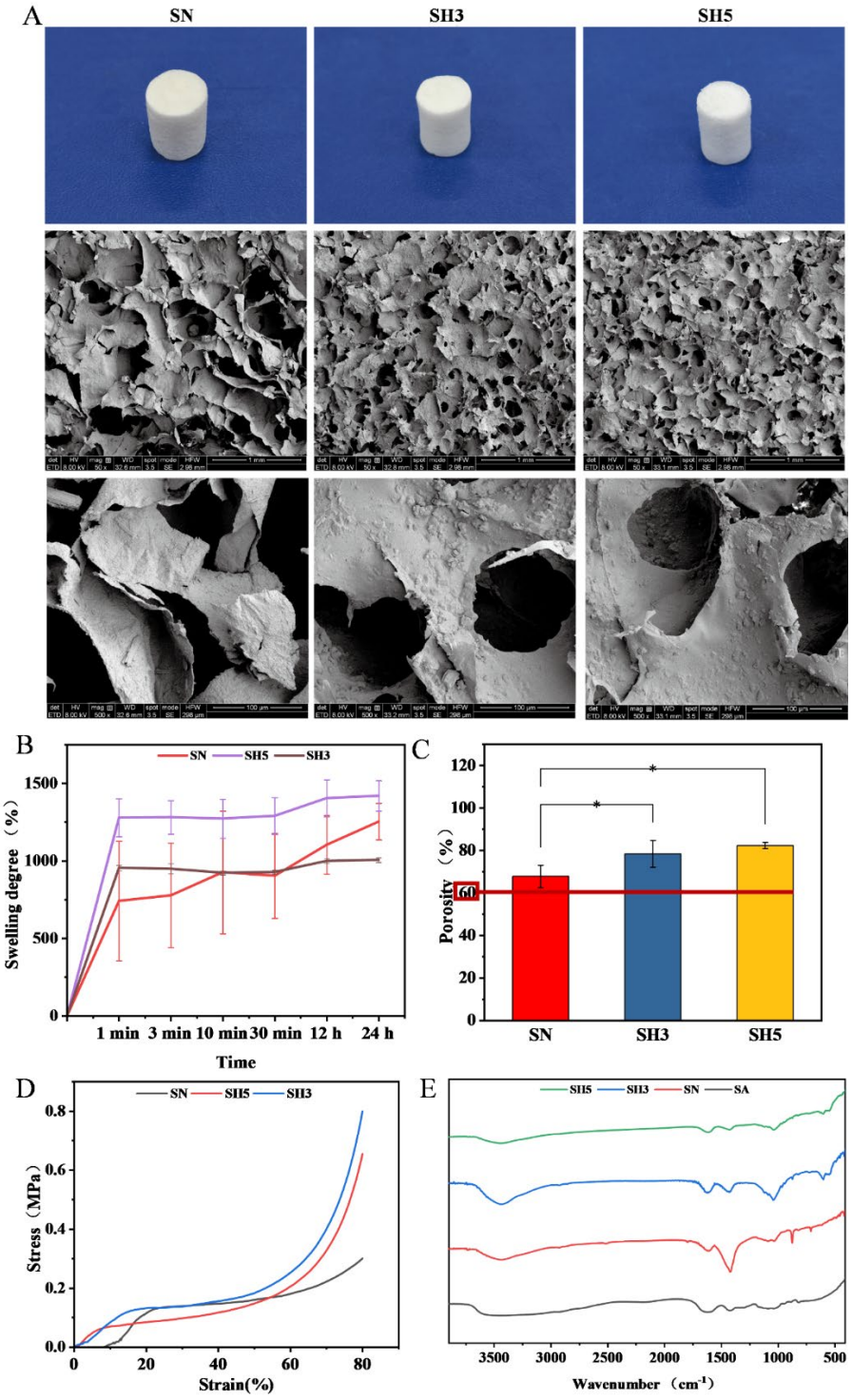

Figure 3. Characterization results of BCP/SA composite scaffolds. **A.** SEM images of composite scaffolds (SN, SH3, and SH5) showing interconnected, sponge-like porous structures with pore sizes ranging from 90 to 120 μm. **B.** Swelling behavior of BCP/SA composite scaffolds over time. The SH3 and SH5 groups reached equilibrium at 1 minute, while the SN group continued to swell. **C.** Porosity of BCP/SA composite scaffolds. The SN, SH3, and SH5 groups exhibited porosities of 67%, 78%, and 82%, respectively. **D.** Compressive stress-strain curves of composite scaffolds. SH3 and SH5 exhibited significantly higher compressive stresses (0.79 MPa and 0.65 MPa) compared to SN (0.3 MPa). **E.** FTIR spectra of BCP/SA composite scaffolds. SH3 and SH5 show characteristic peaks of HAP and β-TCP, confirming successful incorporation of these components into the scaffolds.

Figure 3E presented the infrared spectroscopy results for the composite scaffolds. It could be observed that SH3 and SH5 exhibited characteristic PO_4^{3-} peaks of HAP and β-TCP at 562 cm^{-1}, 610 cm^{-1}, and 1050 cm^{-1}. SN also showed a characteristic CO_3^{2-} peak at 1475 cm^{-1}. Compared to the infrared spectrum of SA, all the infrared spectra of the composite scaffolds contained not only the characteristic peaks of SA but also the characteristic peaks of Nacre, HAP, and β-TCP. These infrared spectroscopy results confirmed the successful fabrication of three composite scaffold materials—SN, SH3, and SH5—using Nacre, H3, H5, and SA.

3.3. Effects of BCP/SA composite scaffolds on MC3T3-E1 adherence and proliferation

Live/dead cell staining results were presented in Figure 4A. Cells were observed to distribute uniformly across all composite scaffold groups, with clear evidence of adhesion and proliferation. After 5 days of culture, the number of cells markedly increased compared to day 3. Green fluorescence signified viable cells, while red fluorescence indicated non-viable cells. Only a minimal number of red-stained cells were detected, suggesting that the composite scaffolds possessed favorable cytocompatibility and effectively supported cell adhesion and growth.

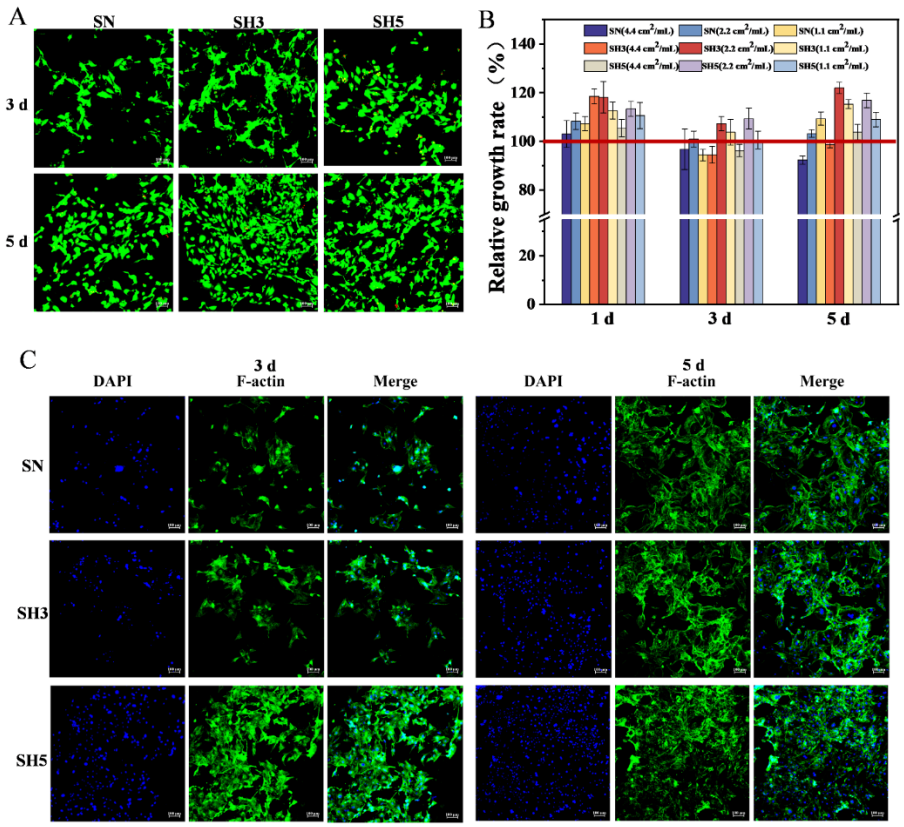

Figure 4. Cytocompatibility and cell proliferation on BCP/SA composite scaffolds. **A.** Live/dead staining of MC3T3-E1 cells after 5 days of culture on composite scaffolds. Green fluorescence indicates live cells, and red fluorescence shows dead cells, demonstrating good cell viability. **B.** Proliferation rates of MC3T3-E1 cells after co-culturing with composite scaffold extracts. The RGR in all experimental groups exceeded 100%, indicating excellent cytocompatibility. **C.** Confocal images of MC3T3-E1 cells on composite scaffolds after 3 and 5 days of culture. The cells show good adhesion and spread morphology, with more cells observed in the SH5 group.

The cytocompatibility of the scaffold leachates was further assessed by MTT assay, as shown in Figure 4B. Following co-culture for 1, 3, and 5 days, cell proliferation in all experimental groups consistently exceeded that of the control group, with relative proliferation rates above 100%. These findings further confirm that the composite scaffolds exhibit excellent biocompatibility and promote cell viability.

According to SEM results, the interior of the composite scaffolds exhibited an interconnected, rough porous structure that provided a surface for MC3T3-E1 cell attachment. After seeding cells onto the scaffold surface and culturing them for 3 and 5 days, cell nuclei and F-actin were stained using DAPI and A488. Blue fluorescence indicated cell nuclei, while green fluorescence indicated actin. The confocal laser microscopy results are shown in Figure 4C. MC3T3-E1 cells attached and grew on the surface of the composite scaffolds, displaying a spread morphology with multiple pseudopods extending from the cells. Cell numbers increased significantly from day 3 to day 5. The SH5 group showed notably more cells than the SH3 and SN groups. The cytoskeleton staining results indicated that the composite scaffolds provided a favorable template for cell adhesion and proliferation.

3.4. Effects of BCP/SA composite scaffolds on the osteogenic activities of MC3T3-E1 cells

Alkaline phosphatase (ALP) is a marker enzyme for early osteoblast differentiation, reflecting the function and activity of osteoblasts. It promotes mineral deposition and plays a crucial role in hard tissue formation. After co-culturing the leaching solutions of composite scaffold with cells for 7 days, ALP expression was observed through staining, as shown in Figure 5A. Figure 5(A1,A2) shows ALP expression both within MC3T3-E1 cells and in intercellular spaces. After 14 days of culture, the ALP staining area and intensity significantly increased in all experimental groups, being notably higher than in the control group. The ALP expression level in the SH5 group was significantly higher compared to the SH3 and SN groups. The results of the ALP activity assay were shown in Figure 5A3. After 7 days of co-culture, ALP activity in the SH5 group was significantly higher than that in the control group. By day 14, ALP activity had further increased across all experimental groups, with statistically significant differences compared to the control group. Among them, the SH5 group exhibited the highest ALP activity. These results indicate that the leachates derived from the composite scaffolds effectively promote osteogenic differentiation of MC3T3-E1 cells, with SH5 exerting the most pronounced effect.

Calcium ions precipitate under ALP activity to form mineralization, with mineralization nodules indicating mature osteogenic differentiation. Figure 5B showed the Alizarin Red S (ARS) staining results after co-culturing cells with leaching solutions of composite scaffold for 14 and 21 days. After 14 days, no noticeable mineralization nodules were observed in either the experimental or control groups. However, significant mineralization nodules appeared in all experimental groups after 21 days. Quantitative analysis of dissolved mineralization nodules, measured by OD540 nm, was shown in Figure 5B3. After 14 days, no significant differences in OD540 nm values were observed between groups. After 21 days, OD values increased in all groups, with mineralization nodules present. The degree of mineralization in the experimental groups was significantly higher than in the control group and the SH5 group showed significant differences compared to the SH3, SN, and control groups. These results indicate that the composite scaffold induced calcium deposition and promoted biomineralization.

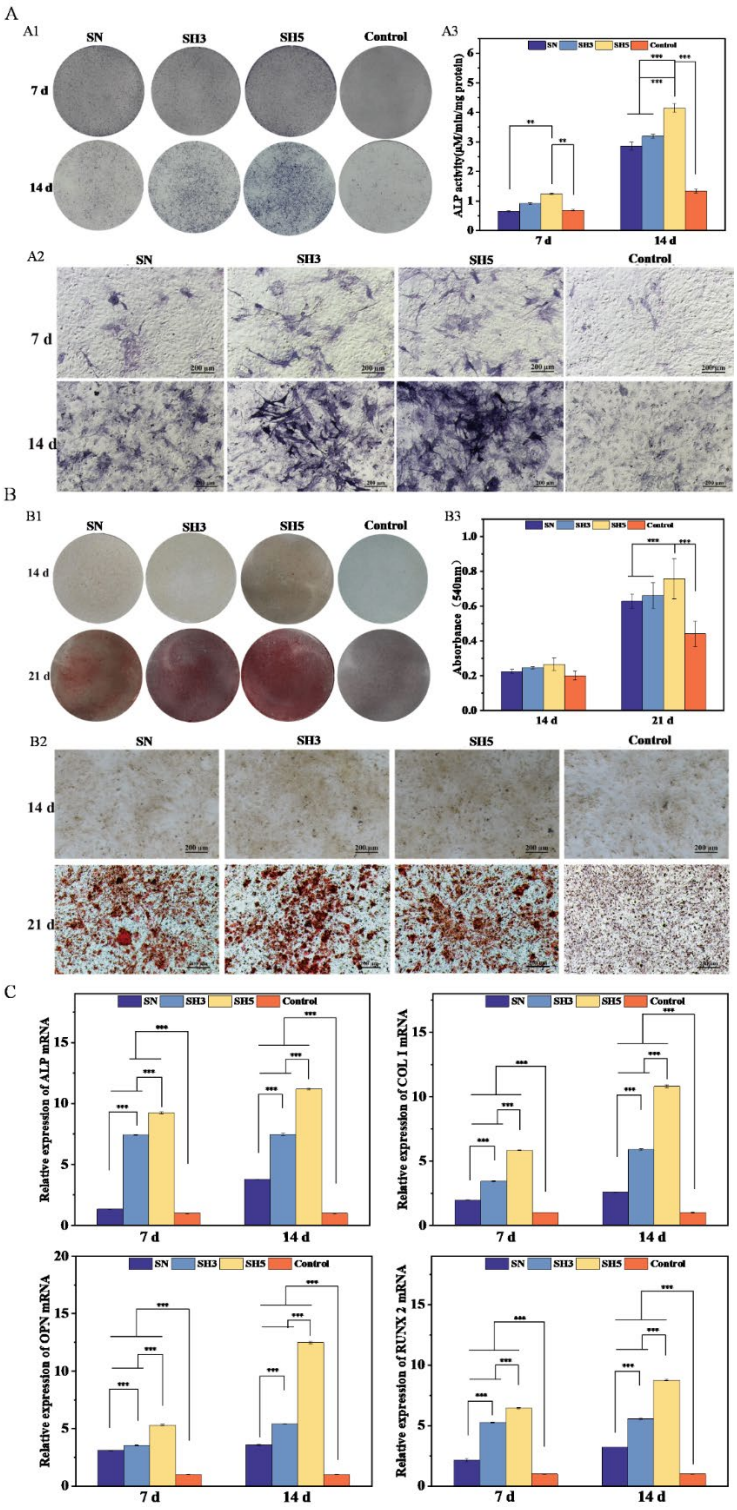

Figure 5. Osteogenic activity of BCP/SA composite scaffolds on MC3T3-E1 cells. **A.** Alkaline phosphatase (ALP) staining of MC3T3-E1 cells after 7 and 14 days of culture with composite scaffold extracts. (A1: digital photographs of the whole well; A2: micrographs of representative area; A3: The relative activity of alkaline phosphatase after 7, and 14 days of coculture). **B.** Alizarin Red S staining for calcium deposition after 14 and 21 days of culture. The SH5 group showed a significantly higher level of mineralization compared to other groups. (B1: digital photographs of the whole well; B2: micrographs of representative area; B3: OD values at 540 nm for alizarin red quantitative measurement). **C.** Real-time PCR analysis of osteogenic genes (ALP, COL-1, OPN, and RUNX-2) in MC3T3-E1 cells after 7 and 14 days of culture. The SH5 group demonstrated the highest expression of osteogenic genes.

To further investigate the effect of composite scaffolds on osteogenic differentiation, we measured the levels of osteogenesis-related genes (*ALP, COL-1, OPN*, and *RUNX-2*) in MC3T3-E1 cells after co-culture with scaffold extracts for 7 and 14 days, using GAPDH as an internal reference gene. The real-time quantitative PCR results were shown in Figure 5C. Type I collagen is the earliest expressed extracellular matrix protein and functions as a key component of the bone matrix to stimulate osteoblast adhesion and provide sites for mineral deposition and calcium nodule formation [45,46]. *RUNX-2*, a crucial transcription factor in early osteogenic differentiation, regulates the transcription of genes such as *COL-1* and *OCN*, promoting osteoblast maturation [47]. As shown in Figure 5, all experimental groups exhibited significantly higher expression levels of *COL-1* and *RUNX-2* genes in MC3T3-E1 cells compared with the blank group. After 14 days of co-culture, *COL-1* and *RUNX-2* expression further increased in the experimental groups relative to day 7, whereas no significant changes were observed in the control group. Among the tested scaffolds, the SH5 group demonstrated the highest gene expression levels, followed by SH3 and SN. These results suggest that the composite scaffolds effectively promote early osteogenic differentiation of MC3T3-E1 cells, with the degree of stimulation ranked as SH5 > SH3 > SN.

Figure 5C also showed that, compared to the control group, experimental groups exhibited significantly increased *ALP* gene expression. OPN, a sulfated and phosphorylated glycoprotein, serves as a major non-collagenous protein in bone tissue and a marker of mature osteoblast differentiation [48]. The SH5 group showed significantly higher *OPN* gene expression compared to the other groups, with a threefold increase at 14 days compared to 7 days. In summary, composite scaffold extracts, especially SH5, significantly promoted the expression of osteogenesis-related genes and demonstrated strong osteoinductive activity. The superior osteoinductive effect of SH5 may be attributed to its higher HAP content compared to SH3.

3.5. Effects of BCP/SA composite scaffolds on HUVEC cell activities

During bone defect repair, cell migration to the defect site was crucial for new bone regeneration. An ideal bone repair material should promote HUVEC cell migration to the defect site, facilitating vascularization and nutrient transport. Vascularization and osteoinductive activity work synergistically to enhance new bone regeneration. The effects of leaching solutions of the composite scaffold on HUVEC cell activity were shown in Figure 6. Figure 6A illustrated the effect of composite scaffold extracts on the two-dimensional migration of HUVEC cells. Figure 6B presents the quantitative statistical results of the cell migration area. The results indicated that the leaching solutions of composite scaffold promoted HUVEC cell migration. After 12 h, the migration rates of cells in the SN, SH3, and SH5 groups reached approximately 50%. At 24 h, cell migration continued in all experimental groups, with the SH5 group showing nearly complete coverage of the scratch area. Compared to the blank group, all experimental groups demonstrated significant cell migration-promoting activity.

Figure 6C showed the effect of leaching solutions of composite scaffold on the three-dimensional migration of HUVEC cells. Figure 6D presented the quantitative statistical results. The Transwell chamber migration assay demonstrated that after 12 h of incubation, cells migrated to the lower chamber, with the number of migrating cells in experimental groups significantly higher than in the control group. SH5 exhibited the strongest cell migration-inducing effect. This study suggested that the composite scaffold can induce cell migration to the defect site, potentially promoting new bone regeneration in the defect area.

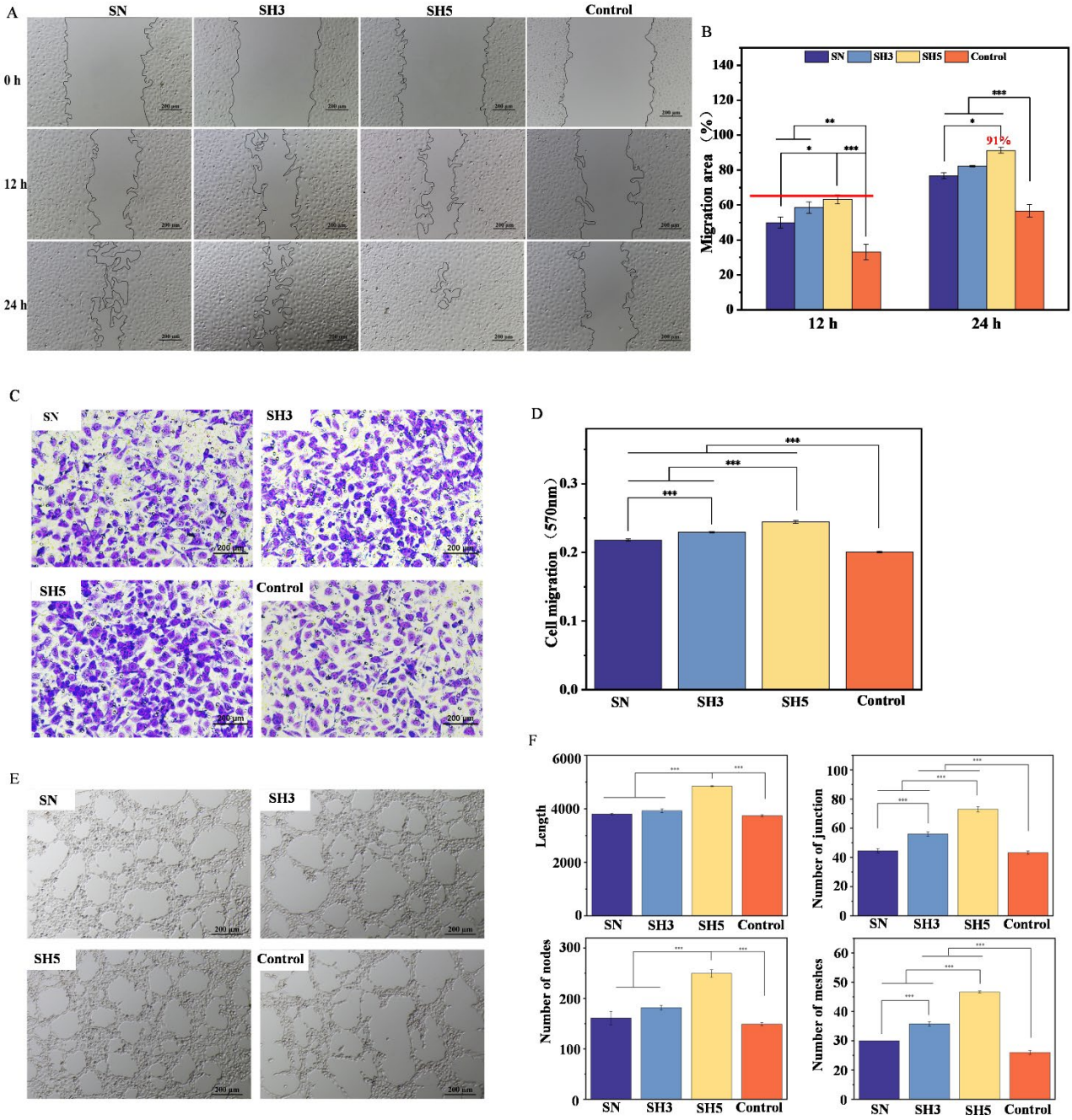

Figure 6. Effects of BCP/SA composite scaffolds on HUVEC cell activities. **A.** The two-dimension migration results after HUVEC was incubated in leaching solutions of composite scaffold for 0 h, 12 h, 24 h. **B.** The quantitative analysis of two-dimension migration results after HUVEC was continuously incubated in leaching solutions of composite scaffold for 12 h, 24 h. **C.** The crystal violet staining results after HUVEC was incubated in each group of composite scaffold extracts for 12 h. **D.** The quantitative detection of the 3D migration after HUVEC was continuously incubated in each group of composite scaffold extracts for 12 h. **E.** The effects of each group of composite scaffolds on tube formation of HUVEC *in vitro*. **F.** The quantified results of nodes, meshes, junctions and tube length of HUVEC treated with composite scaffolds *in vitro*.

Blood vessels play a critical role in new bone formation [49]. During bone tissue repair, bone vascularization and regeneration are coupled, with good vascular regeneration positively affecting new

bone regeneration [50,51]. The effect of leaching solutions of composite scaffold on HUVEC *in vitro* angiogenesis was shown in Figure 6E. Quantitative analysis of vessel nodes, meshes, junctions, and vessel length of HUVEC cells in Figure 6E using ImageJ were shown in Figure 6F. The results revealed that the SH5 group exhibited highly significant differences in the number of vessel nodes, meshes, vessel length, and junctions compared to other experimental groups and the control group. The SN group showed no significant *in vitro* angiogenic activity.

3.6. Effects of BCP/SA composite scaffolds on rat cranial defects repair

The three-dimensional reconstruction and cross-sectional Micro-CT images of rat skulls at 1, 2, and 3 months after implantation of composite BCP/SA scaffold materials in cranial defects were shown in Figure 7A,B. New bone growth was observed along the margins of the bone defects at different time points post-implantation. At 1 month, minimal new bone formation was observed in the SN and SH3 groups, while the SH5 group showed more new bone tissue, with irregular bone formation visible at the defect margins. At 2 months, the SH5 group exhibited notably more new bone formation compared to the other groups. At 3 months, the SH5 group displayed new bone formation not only along the defect margins but also punctate bone formation in the central defect area, indicating that SH5 provided an effective scaffold for new bone growth, offering attachment sites for osteoblasts and facilitating calcium matrix deposition. The SN and SH3 groups showed only minimal new bone tissue formation. Cross-sectional analysis revealed that new bone growth consistently initiated from the margins. The SH5 composite scaffold demonstrated superior regenerative performance in rat cranial defect repair compared with the SH3 and SN groups, suggesting that the hydroxyapatite (HAP) to β-tricalcium phosphate (β-TCP) ratio in the SH5 biphasic calcium phosphate formulation provided a more favorable composition. Micro-CT analysis of bone specimens at 3 months post-implantation, including bone volume fraction (BV/TV), bone surface area to bone volume ratio (BS/BV), and bone mineral density (BMD), is summarized in Table 2. The results revealed that the SH5 group exhibited significantly greater BV/TV and BMD values relative to the SH3, SN, and control groups, confirming its enhanced osteogenic potential.

Table 2. The bone tissue parameters of cranial in 3 months.

3 M	BV/TV (%)	BS/BV (mm^{-1})	BMD (mg/cc)
SN	14.1	11.19	1.25
SH3	16.3	9.96	1.75
SH5	28.99	6.37	2.25
Control	14.86	8.24	1.03

Histopathological examination was performed on bone tissue samples at different time points. The H&E staining results were shown in Figure 7C. At 1 month post-surgery, no inflammatory cells such as neutrophils or macrophages were observed in either the blank or experimental groups. The blank group's defect area was covered by a thin layer of connective tissue, while the experimental groups showed connective tissue infiltration into the composite scaffolds. The defect margins in all experimental groups became irregular, with varying degrees of new bone growth. A layer of osteoblasts surrounded and aligned along the defect surface. At 3 months post-surgery, further new bone formation was observed in

all experimental groups. In the SH5 group, new bone growth from both terminals had nearly connected, with new bone formation occurring not only along the defect margins but also in the central defect area.

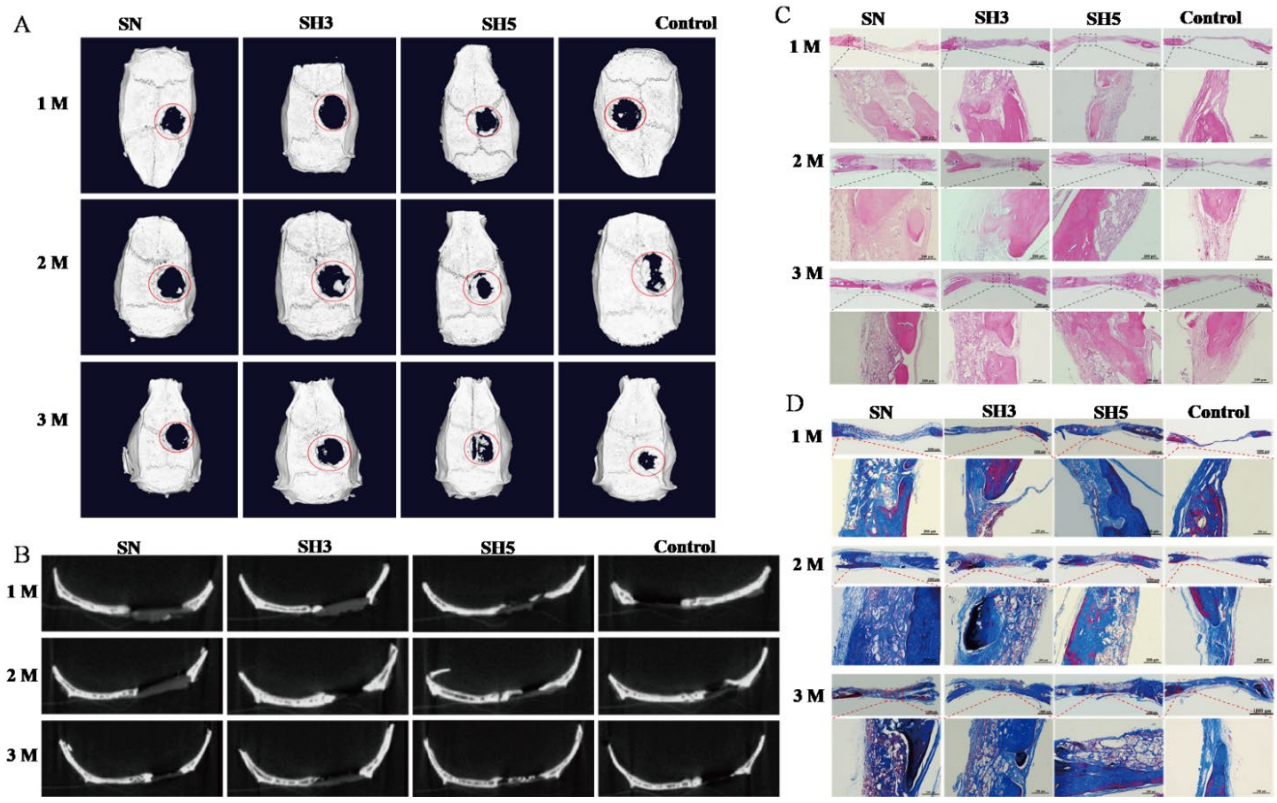

Figure 7. *In vivo* bone defect repair using BCP/SA composite scaffolds. **A.** 3D reconstruction of rat cranial defects at 1, 2 and 3 months post-implantation. The SH5 group showed the most significant new bone formation at all time points. **B.** Cross-sectional Micro-CT images of cranial defects at 1, 2, and 3 months. SH5 demonstrated superior bone healing compared to SH3 and SN groups. **C.** H&E staining of rat cranial defect tissues at different time points, showing new bone formation and integration with the scaffold in the SH5 group. **D.** Masson's trichrome staining of rat cranial defect tissues, highlighting collagen formation in the SH5 group by 3 months post-surgery.

Masson staining of cranial tissue sections at various time points were shown in Figure 7D. At 1 month post-surgery, collagen formation was observed in the bone defect area of all experimental groups. The blue-stained collagen also encapsulated the composite scaffold surface. At this time, the scaffold still maintained its intact shape and continued to provide support, without obvious degradation. At 2 months, matrix mineralization occurred, with good integration between the scaffold material and new bone tissue. New bone tissue formed both within the composite scaffold and grew outward from the old bone surface. The initial degradation of the material is replaced by new bone tissue and provides space for the expansion of new bone. At 3 months, the scaffold materials in the SH5 group had degraded and been replaced by new bone. The two defect margins were essentially connected, with high-density collagen present. Masson staining results indicated that collagen formed within the composite scaffold, likely due to the scaffold's internal porous structure providing surfaces for cell infiltration, adhesion, and proliferation. Osteoblasts generated within the scaffold material secrete collagen, promoting the formation of new bone tissue and further facilitating the degradation of the material. Bone repair is a long-term

process. Residual scaffolds can provide support and guidance for new bone when necessary, ultimately achieving a degradation-regeneration coupling that matches the maturation process of new bone tissue.

3.7. Immunofluorescence staining analysis of rat calvarial defect model

The immunofluorescence staining results of tissue sections from the rat calvarial defect model at 3 months were shown in Figure 8. Osteocalcin (OCN) is a marker of osteoblast differentiation and maturation, playing a crucial role in attracting and binding calcium ions, promoting calcium deposition, and bone calcification. The expression level of OCN can reflect the activity of osteoblasts and the capacity for bone formation. The immunofluorescence staining results for OCN were shown in Figure 8A,D. The SH5 and SH3 groups showed obvious positive OCN expression, and the SH5 group had the strongest fluorescence signal, which was widely distributed in the new bone tissue and the defect center area. This indicated that the SH5 group had the highest bone formation activity and the most significant osteogenic effect. Additionally, the expression of OCN was positively correlated with the expression of other osteogenic markers such as Runx2 and ALP, further validating its role in bone formation.

Osteopontin (OPN) is a multifunctional protein involved in both bone resorption and bone formation processes. During bone defect repair, the expression level of OPN can reflect the balance between bone resorption and bone formation. The immunofluorescence staining results for OPN were shown in Figure 8B,D. The SN and control groups exhibited weak OPN expression, indicating insufficient bone matrix maturity and incomplete repair. The SH3 group showed enhanced OPN expression, with widespread green fluorescence distribution. The SH5 group exhibited the strongest OPN expression, indicating the highest activity of both bone resorption and bone formation.

Osteoprotegerin (OPG) is primarily expressed by osteoblasts and osteoclast precursor cells in bone tissue. By competitively binding with RANKL, OPG inhibits the activation of osteoclasts and bone resorption. The immunofluorescence staining results for OPG were shown in Figure 8C,D. The expression area of OPG in the SH5 and SH3 groups was significantly higher than that in the SN and control groups, indicating that HAP and β-TCP significantly promote bone regeneration at the defect site. In the SH3 group, green fluorescence was mainly located at the edges of the defect, with sparse distribution in the central area. In contrast, the SH5 group showed widespread green fluorescence distribution at both the edges and the center of the bone defect.

In summary, the SH5 group demonstrated the best bone formation and bone resorption inhibition effects in bone defect repair, followed by the SH3 group, while the SN and control groups showed poorer bone repair effects. These results indicated that the BCP/SA composite scaffolds, particularly the SH5, has significant bone repair potential and can effectively enhance bone defect repair.

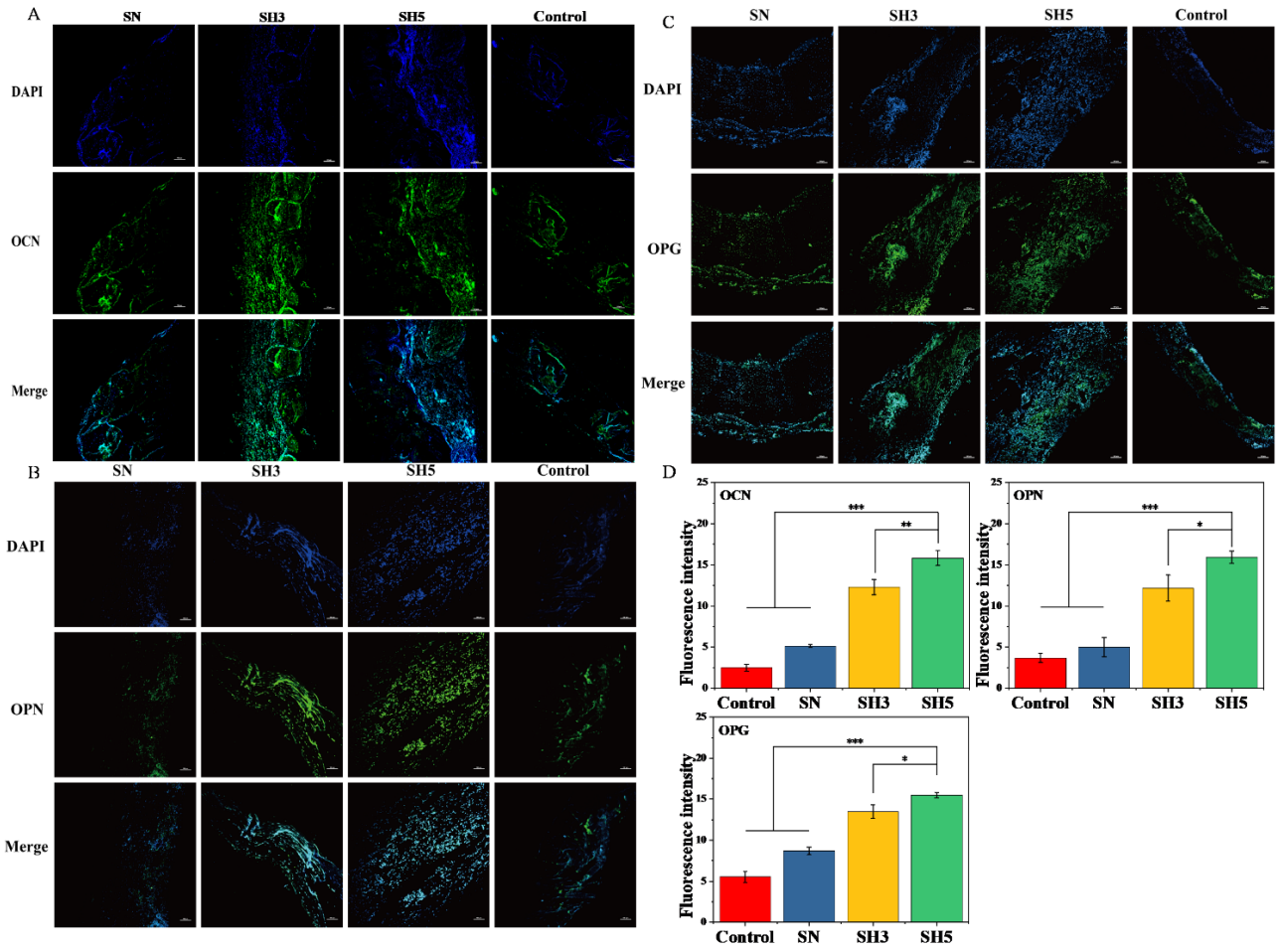

Figure 8. Immunofluorescence staining of rat cranial defect tissues. **A.** Immunofluorescence staining of osteocalcin (OCN) in rat cranial defect tissues. The SH5 group exhibited the strongest OCN expression, indicating active bone formation. **B.** Immunofluorescence staining of osteopontin (OPN), showing higher expression in the SH5 group, indicative of enhanced osteogenesis. **C.** Immunofluorescence staining of osteoprotegerin (OPG), showing significant expression in the SH5 and SH3 groups, suggesting effective bone regeneration and resorption regulation. **D.** Quantitative measurement of OCN-, OPN-, and OPG-stained fluorescence images at 3 months after surgery.

4. Discussion and conclusion

Bone repair materials must possess specific characteristics, including a suitable porous structure, pore size, and biological activity to facilitate tissue growth and regeneration. The ideal pore size for bone scaffolds is generally designed between 100–300 μm, allowing for cell infiltration, migration, and growth. This range has been shown to support vascularization and aid in bone tissue formation by ensuring the effective diffusion of oxygen and nutrients, as well as the removal of metabolic waste [52,53]. Studies have suggested that scaffolds with pore sizes ranging from 200 to 350 μm may be optimal for tissue integration, while smaller pores around 100 μm facilitate osteoblast differentiation and bone formation in repairing flat bone defects. These characteristics are critical for the success of bone tissue engineering, where scaffolds provide a supportive environment for the growth of new bone tissue [54]. The biological functionality of bone repair materials is essential to their performance *in vivo*. Osteogenesis,

osteoconduction, and osteoinduction are three key properties required for successful bone repair [55,56]. These biological functions, combined with proper material characteristics, define the effectiveness of a bone repair scaffold.

Our study aimed to assess the osteo-inductive and angiogenic properties of BCP/SA composite scaffolds. Previous research has demonstrated the osteo-inductive and angiogenic properties of biphasic calcium phosphate (BCP) scaffolds. Anghelescu *et al.* found that BCP bone substitutes significantly promoted angiogenesis in animal models, showing that HAP could act as a matrix supporting capillary development [57]. The BCP/SA scaffolds in our study demonstrated similar findings, with SH5, which had a higher HAP ratio, showing the most significant osteo-inductive and angiogenic effects.

In line with the findings of Shie M.Y. and colleagues, the Ca^{2+} concentration in the composite scaffold plays a crucial role in osteoinduction [58]. Calcium ions, which are released during the degradation of materials like β-TCP, stimulate osteoblast proliferation and differentiation [59,60]. However, high concentrations of Ca^{2+} (above 10 mM) will exert cytotoxicity [61]. In our study, the varying ratios of HAP and β-TCP in the composite scaffolds influenced the calcium ion release and, consequently, the osteo-inductive activity of the scaffolds. SH5, with a balanced HAP:β-TCP ratio, exhibited a higher osteo-inductive activity, likely due to its enhanced calcium ion release, which promoted osteoblast differentiation. The SH3 group, which had a higher β-TCP content (70%), showed lower osteogenic and osteo-inductive activity than the SH5 group. This is consistent with previous studies, such as those by Ghanaati *et al.*, which indicated that β-TCP, while promoting bone conduction, might not have the same osteo-inductive effects as HAP. β-TCP's rapid degradation can enhance bone conduction but may not support sufficient cell attachment and differentiation, thereby limiting its osteo-inductive potential. This mismatch could explain the lower bone formation observed in the SH3 group compared to SH5. This result highlights the importance of the HAP:β-TCP ratio in optimizing the material's biological functions.

In conclusion, the BCP/SA composite scaffolds in this study demonstrated promising potential for bone repair, particularly SH5, which exhibited superior osteoinductive properties. The combination of HAP and β-TCP in optimized ratios enhances both osteoblast activity and angiogenesis, making the SH5 scaffold a promising material for bone tissue engineering. However, further optimization of the degradation rates of BCP/SA may be necessary to improve scaffold-tissue integration and the long-term success of bone regeneration.

Acknowledgments

This work was financially supported by the Open Fund of Key Laboratory of Biotechnology and Bioresources Utilization (No. KF2021004), and Qingdao Municipal Science and Technology Bureau (No. 23-1-4-xxgg-4-gx).

Authors' contribution

Conceptualization, Yan Yang; methodology, Wenli Dong and Lujing Zhang; software, Kaisheng Wang and Yu Zhang; validation, Lujing Zhang and Yanni Li; formal analysis, Wenli Dong, Lujing Zhang and Yu Zhang; investigation, Wenli Dong and Lujing Zhang; data curation, Kaisheng Wang; writing—original draft preparation, Wenli Dong; writing—review and editing, Lujing Zhang and Yan Yang; visualization, Kaisheng Wang and Yanni Li; supervision, Yan Yang and Chao Zhou; project administration, Yan Yang

and Chao Zhou; funding acquisition, Yan Yang. All authors have read and agreed to the published version of the manuscript.

Conflicts of interests

The authors declare no conflict of interest.

Ethical statement

The study was approved by the Animal Ethics Committee of Ocean University of China (OUC) (Approval number: OUC-AE-2022-167). All experiments were conducted in accordance with the institutional guidelines for the care and use of laboratory animals. Direct quotations from another author's work should be cited as footnote. For publications that are Accepted or submitted or in preparation, please just add a note at the end of the corresponding reference.

References

[1] Koons GL, Diba M, Mikos AG. Materials design for bone-tissue engineering. *Nat. Rev. Mater.* 2020, 5:584–603.

[2] Matić S, Vučković Č, Lešić A, Glišović Jovanović I, Polojac D, *et al.* Pedicled vascularized bone grafts compared with xenografts in the treatment of scaphoid nonunion. *Int. Orthop.* 2021, 45:1017–1023.

[3] Nudelman F, Shimoni E, Klein E, Rousseau M, Bourrat X, *et al.* Forming nacreous layer of the shells of the bivalves Atrina rigida and Pinctada margaritifera: an environmental-and cryo-scanning electron microscopy study. *J. Struct. Biol.* 2008, 162:290–300.

[4] Stempflé P, Bourrat X, Rousseau M, Lopez E, Takadoum J. Nanotribology of nacre: anisotropic dissipation in a multiscale hybrid material. *Tribol. Int.* 2013, 63:250–264.

[5] Feng P, Zhao R, Tang W, Yang F, Tian H, *et al.* Structural and functional adaptive artificial bone: materials, fabrications, and properties. *Adv. Funct. Mater.* 2023, 33:2214726.

[6] Barthelat F, Tang H, Zavattieri PD, Li CM, Espinosa HD. On the mechanics of mother-of-pearl: a key feature in the material hierarchical structure. *J. Mech. Phys. Solids* 2007, 55:306–337.

[7] Reddy VS, Surakanti JR, Sharma DK. A comparative evaluation of human enamel remineralization ability of biomimetic nacre against casein phosphopeptide-amorphous calcium phosphate: an *in vitro* study. *J. Conserv. Dent. Endod.* 2024, 27:954–961.

[8] Atlan G, Balmain N, Berland S, Vidal B, Lopez É. Reconstruction of human maxillary defects with nacre powder: histological evidence for bone regeneration. *Comptes Rendus de l'Académie des Sciences-Series III-Sciences de la Vie* 1997, 320:253–258.

[9] Kobayashi S, Ui M, Araikawa H, Sakamoto T, Nakai K. Effect of heat treatments of bioactive nacre on HAp formation in SBF. *Mater. Sci. Forum* 2012, 706–709:526–531.

[10] Ruan R, Heidari BS, Chen PL, Gao JJ, Chen ZM, *et al.* Converting ocean nacre into bone mineral matrix composite for bone regeneration-and *in vivo* studies. *Mater. Des.* 2024, 245:113271.

[11] Wu SC, Hsu HC, Hsu SK, Tseng CP, Ho WF. Effects of calcination on synthesis of hydroxyapatite derived from oyster shell powders. *J. Aust. Ceram. Soc.* 2019, 55:1051–1058.

[12] Wu SC, Hsu HC, Wu YN, Ho WF. Hydroxyapatite synthesized from oyster shell powders by ball milling and heat treatment. *Mater. Charact.* 2011, 62:1180–1187.

[13] Afewerki S, Bassous N, Harb S, Palo-Nieto C, Ruiz-Esparza GU, *et al.* Advances in dual functional antimicrobial and osteoinductive biomaterials for orthopaedic applications. *Nanomedicine* 2020, 24:102143.

[14] Ma B, Han J, Zhang S, Liu F, Wang S, *et al.* Hydroxyapatite nanobelt/polylactic acid Janus membrane with osteoinduction/barrier dual functions for precise bone defect repair. *Acta Biomater.* 2018, 71:108–117.

[15] Chen W, Oh S, Ong AP, Oh N, Liu Y, *et al.*Antibacterial and osteogenic properties of silver-containing hydroxyapatite coatings produced using a sol gel process. *J. Biomed. Mater. Res. A* 2007, 82:899–906.

[16] Hashimoto K, Oikawa H, Shibata H. Characterization of porous β-type tricalcium phosphate ceramics formed via physical foaming with freeze-drying. *Int. J. Mol. Sci.* 2024, 25(10):5363.

[17] Bohner M, Santoni BLG, Döbelin N. β-tricalcium phosphate for bone substitution: synthesis and properties. *Acta Biomater.* 2020, 113:23–41.

[18] Rojbani H, Nyan M, Ohya K, Kasugai S. Evaluation of the osteoconductivity of α-tricalcium phosphate, β-tricalcium phosphate, and hydroxyapatite combined with or without simvastatin in rat calvarial defect. *J. Biomed. Mater. Res. A* 2011, 98:488–498.

[19] Cheng L, Yan S, Zhu J, Cai P, Wang T, *et al.* Exercise enhance the ectopic bone formation of calcium phosphate biomaterials in muscles of mice. *Mater. Sci. Eng. C* 2017, 77:136–141.

[20] Bohner M, Baroud G, Bernstein A, Döbelin N, Galea L, *et al.* Characterization and distribution of mechanically competent mineralized tissue in micropores of β-tricalcium phosphate bone substitutes. *Mater. Today* 2017, 20:106–115.

[21] Tanaka T, Saito M, Chazono M, Kumagae Y, Kikuchi T, *et al.* Effects of alendronate on bone formation and osteoclastic resorption after implantation of beta-tricalcium phosphate. *J. Biomed. Mater. Res. A* 2010, 93:469–474.

[22] Davison NL, ten Harkel B, Schoenmaker T, Luo X, Yuan H, *et al.* Osteoclast resorption of beta-tricalcium phosphate controlled by surface architecture. *Biomaterials* 2014, 35:7441–7451.

[23] Chazono M, Tanaka T, Kitasato S, Kikuchi T, Marumo K. Electron microscopic study on bone formation and bioresorption after implantation of β-tricalcium phosphate in rabbit models. *J. Orthop. Sci.* 2008, 13:550–555.

[24] Ogose A, Kondo N, Umezu H, Hotta T, Kawashima H, *et al.* Histological assessment in grafts of highly purified beta-tricalcium phosphate (OSferion) in human bones. *Biomaterials* 2006, 27:1542–1549.

[25] Tanaka T, Komaki H, Chazono M, Kitasato S, Kakuta A, *et al.* Basic research and clinical application of beta-tricalcium phosphate (β-TCP). *Morphologie* 2017, 101:164–172.

[26] No YJ, Li JJ, Zreiqat H. Doped calcium silicate ceramics: a new class of candidates for synthetic bone substitutes. *Materials* 2017, 10(2):153.

[27] Mofakhami S, Salahinejad E. Biphasic calcium phosphate microspheres in biomedical applications. *J. Controlled Release* 2021, 338:527–536.

[28] Lin Y, Fu ML, Harb I, Ma LX, Tran SD. Functional biomaterials for local control of orthodontic tooth movement. *J. Funct. Biomater.* 2023, 14(6):294.

[29] Wang Z, Sun Y, Li C. Advances in 3D printing technology for preparing bone tissue engineering scaffolds from biodegradable materials. *Front. Bioeng. Biotechnol.* 2024, 12:1483547.

[30] Brochu BM, Sturm SR, Kawase De Queiroz Goncalves JA, Mirsky NA, Sandino AI, *et al.* Advances in bioceramics for bone regeneration: a narrative review. *Biomimetics (Basel)* 2024, 9(11):690.

[31] Sharma C, Dinda AK, Potdar PD, Chou CF, Mishra NC. Fabrication and characterization of novel nano-biocomposite scaffold of chitosan–gelatin–alginate–hydroxyapatite for bone tissue engineering. *Mater. Sci. Eng. C* 2016, 64:416–427.

[32] Cao L, Lu W, Mata A, Nishinari K, Fang Y. Egg-box model-based gelation of alginate and pectin: a review. *Carbohydr. Polym.* 2020, 242:116389.

[33] Bhattarai N, Li Z, Edmondson D, Zhang M. Alginate-based nanofibrous scaffolds: structural, mechanical, and biological properties. *Adv. Mater.* 2006, 18(11):1463–1467.

[34] Fernando IPS, Lee W, Han EJ, Ahn G. Alginate-based nanomaterials: fabrication techniques, properties, and applications. *Biochem. Eng. J.* 2020, 391:123823.

[35] Chae T, Yang H, Leung V, Ko F, Troczynski T. Novel biomimetic hydroxyapatite/alginate nanocomposite fibrous scaffolds for bone tissue regeneration. *J. Mater. Sci.: Mater. Med.* 2013, 24:1885–1894.

[36] Zhao L, Weir MD, Xu HHK. An injectable calcium phosphate-alginate hydrogel-umbilical cord mesenchymal stem cell paste for bone tissue engineering. *Biomaterials* 2010, 31:6502–6510.

[37] Lee GS, Park JH, Won JE, Shin US, Kim HW. Alginate combined calcium phosphate cements: mechanical properties and *in vitro* rat bone marrow stromal cell responses. *J. Mater. Sci. Mater. Med.* 2011, 22:1257–1268.

[38] Wu Z, Meng Z, Wu Q, Zeng D, Guo Z, *et al.* Biomimetic and osteogenic 3D silk fibroin composite scaffolds with nano MgO and mineralized hydroxyapatite for bone regeneration. *J. Tissue Eng.* 2020, 11:2041731420967791.

[39] Muzzarelli R, Biagini G, Pugnaloni A, Filippini O, Baldassarre V, *et al.* Reconstruction of parodontal tissue with chitosan. *Biomaterials* 1989, 10:598–603.

[40] Liu T, Xu J, Pan X, Ding Z, Xie H, *et al.* Advances of adipose-derived mesenchymal stem cells-based biomaterial scaffolds for oral and maxillofacial tissue engineering. *Bioact. Mater.* 2021, 6:2467–2478.

[41] Arthur A, Gronthos S. Clinical application of bone marrow mesenchymal stem/stromal cells to repair skeletal tissue. *Int. J. Mol. Sci.* 2020, 21(24):9759.

[42] Kelly CN, Miller AT, Hollister SJ, Guldberg RE, Gall K. Design and structure–function characterization of 3D printed synthetic porous biomaterials for tissue engineering. *Adv. Healthcare Mater.* 2018, 7(7):1701095.

[43] He J, Chen G, Liu M, Xu Z, Chen H, *et al.* Scaffold strategies for modulating immune microenvironment during bone regeneration. *Mater. Sci. Eng. C* 2020, 108:110411.

[44] Xu M, Qin M, Zhang X, Zhang X, Li J, *et al.* Porous PVA/SA/HA hydrogels fabricated by dual-crosslinking method for bone tissue engineering. *J. Biomater. Sci. Polym. Ed.* 2020, 31:816–831.

[45] Zha L, Hou N, Wang J, Yang G, Gao Y, *et al.* Collagen1alpha1 promoter drives the expression of Cre recombinase in osteoblasts of transgenic mice. *J. Genet. Genomics* 2008, 35:525–530.

[46] Higgins JA, Ezzell J, Hinnebusch BJ, Shipley M, Henchal EA, *et al.* 5' nuclease PCR assay to detect Yersinia pestis. *J. Clin. Microbiol.* 1998, 36:2284–2288.

[47] Vimalraj S, Arumugam B, Miranda PJ, Selvamurugan N. Runx2: structure, function, and phosphorylation in osteoblast differentiation. *Int. J. Biol. Macromol.* 2015, 78:202–208.

[48] Ririe KM, Rasmussen RP, Wittwer CT. Product differentiation by analysis of DNA melting curves during the polymerase chain reaction. *Anal. Biochem.* 1997, 245:154–160.

[49] ElHawary H, Baradaran A, Abi-Rafeh J, Vorstenbosch J, Xu L, *et al.* Bone healing and inflammation: principles of fracture and repair. *Semin. Plast. Surg.* 2021, 35:198–203.

[50] Zhang H, Zhou Y, Zhang W, Wang K, Xu L, *et al.* Construction of vascularized tissue-engineered bone with a double-cell sheet complex. *Acta Biomater.* 2018, 77:212–227.

[51] Cui H, Zhu W, Nowicki M, Zhou X, Khademhosseini A, *et al.* Hierarchical fabrication of engineered vascularized bone biphasic constructs via dual 3d bioprinting: integrating regional bioactive factors into architectural design. *Adv. Healthc Mater.* 2016, 5:2174–2181.

[52] Prochor P, Gryko A. Numerical analysis of the influence of porosity and pore geometry on functionality of scaffolds designated for orthopedic regenerative medicine. *Materials (Basel)* 2020, 14(1):109.

[53] Di Luca A, Longoni A, Criscenti G, Mota C, van Blitterswijk C, *et al.* Toward mimicking the bone structure: design of novel hierarchical scaffolds with a tailored radial porosity gradient. *Biofabrication* 2016, 8:045007.

[54] Zhao W, Huang Z, Liu L, Wang W, Leng J, *et al.* Porous bone tissue scaffold concept based on shape memory PLA/Fe3O4. *Compos. Sci. Technol.* 2020, 203:108563.

[55] Ding T, Kang W, Li J, Yu L, Ge S. An *in situ* tissue engineering scaffold with growth factors combining angiogenesis and osteoimmunomodulatory functions for advanced periodontal bone regeneration. *J. Nanobiotechnol.* 2021, 19:247.

[56] Chen S, Wang H, Liu D, Bai J, Haugen HJ, *et al.* Early osteoimmunomodulation by mucin hydrogels augments the healing and revascularization of rat critical-size calvarial bone defects. *Bioact. Mater.* 2023, 25:176–188.

[57] Anghelescu VM, Neculae I, Dincă O, Vlădan C, Socoliuc C, *et al.* Inflammatory-driven angiogenesis in bone augmentation with bovine hydroxyapatite, B-tricalcium phosphate, and bioglasses: a comparative study. *J. Immunol. Res.* 2018, 2018(1):9349207.

[58] Remya NS, Syama S, Gayathri V, Varma HK, Mohanan PV. An *in vitro* study on the interaction of hydroxyapatite nanoparticles and bone marrow mesenchymal stem cells for assessing the toxicological behaviour. *Colloids Surf., B* 2014, 117:389–397.

[59] Shie MY, Ding SJ. Integrin binding and MAPK signal pathways in primary cell responses to surface chemistry of calcium silicate cements. *Biomaterials* 2013, 34:6589–6606.

[60] Maeno S, Niki Y, Matsumoto H, Morioka H, Yatabe T, *et al.* The effect of calcium ion concentration on osteoblast viability, proliferation and differentiation in monolayer and 3D culture. *Biomaterials* 2005, 26:4847–4855.

[61] Ciapetti G, Di Pompo G, Avnet S, Martini D, Diez-Escudero A, *et al.* Osteoclast differentiation from human blood precursors on biomimetic calcium-phosphate substrates. *Acta Biomater.* 2017, 50:102–113.